

Probing primordial features with future galaxy surveys

M. Ballardini,^{a,b,c} F. Finelli,^{b,c} C. Fedeli^{a,d,c} and L. Moscardini^{a,d,c}

^aDIFA, Dipartimento di Fisica e Astronomia, Alma Mater Studiorum Università di Bologna, Viale Berti Pichat, 6/2, I-40127 Bologna, Italy

^bINAF/IASF Bologna, via Gobetti 101, I-40129 Bologna, Italy

^cINFN, Sezione di Bologna, Via Berti Pichat 6/2, I-40127 Bologna, Italy

^dINAF/Osservatorio Astronomico di Bologna, Via Ranzani 1, I-40127 Bologna, Italy

E-mail: ballardini@iasfbo.inaf.it, finelli@iasfbo.inaf.it, cosimo.fedeli@gmail.com, lauro.moscardini@unibo.it

Abstract. We study the capability of future measurements of the galaxy clustering power spectrum to probe departures from a power-law spectrum for primordial fluctuations. On considering the information from the galaxy clustering power spectrum up to quasi-linear scales, i.e. $k < 0.1 \text{ h Mpc}^{-1}$, we present forecasts for DESI, Euclid and SPHEREx in combination with CMB measurements. As examples of departures in the primordial power spectrum from a simple power-law, we consider four *Planck* 2015 best-fits motivated by inflationary models with different breaking of the slow-roll approximation. These four representative models provide an improved fit to CMB temperature anisotropies, although not at statistical significant level. As for other extensions in the matter content of the simplest Λ CDM model, the complementarity of the information in the resulting matter power spectrum expected from these galaxy surveys and in the primordial power spectrum from CMB anisotropies can be effective in constraining cosmological models. We find that the three galaxy surveys can add significant information to CMB to better constrain the extra parameters of the four models considered.

Contents

1	Introduction	1
2	Deviations from a simple power law for primordial fluctuations consistent with <i>Planck</i>	3
2.1	Model 1: An exponential cut-off on large scales with variable stiffness	4
2.2	Model 2: Discontinuity in the first derivative of the potential	5
2.3	Model 3: Step in the inflaton potential	5
2.4	Model 4: Logarithmic super-imposed oscillations	6
2.5	Current constraints from CMB	6
3	Combined Forecast for CMB and LSS	7
3.1	Fisher matrix for CMB	8
3.2	Fisher matrix for spectroscopic galaxy surveys	10
4	A selection of future LSS catalogs	11
4.1	Dark Energy Spectroscopic Instrument (DESI)	13
4.2	Euclid	13
4.3	Spectro-Photometer for the History of the Universe, Epoch of Reionization, and Ices Explorer (SPHEREx)	14
5	Results and Discussions	14
6	Conclusions	16

1 Introduction

The results from the ESA satellite *Planck* [1, 2] led to important progresses in the context of inflation [3, 4]. In fact they showed how the theoretical predictions of the simplest slow-roll inflationary models, such as a flat Universe with nearly Gaussian adiabatic perturbations and a tilted spectrum, provide a good fit to CMB temperature and polarization anisotropies. The BICEP 2/Keck Array/*Planck* constraint on the tensor-to-scalar ratio at the scale $k_* = 0.05 \text{ Mpc}^{-1}$ (the energy scale of inflation) as $r < 0.08$ ($V^{1/4} \approx 1.8 \times 10^{16} \text{ GeV}$) at the 95 % confidence level (CL) [5], has allowed to strongly disfavour archetypal models such as a quadratic potential or natural inflation [4]. With the most recent release of the Keck Array 95 GHz, the constraint on primordial gravitational waves has been further tightened to $r < 0.07$ at 95 % CL [6].

Although a spatially flat Λ CDM model with a tilted power-law spectrum of primordial fluctuations provides a good fit to *Planck* data, there are intriguing *features* in the temperature power spectrum, such as a dip at $\ell \sim 20$, a smaller average amplitude at $\ell \lesssim 40$ and other outliers at higher multipoles. The features at $\ell \lesssim 40$ in the CMB temperature power spectrum generate a particular pattern at $k \lesssim 0.008 \text{ Mpc}^{-1}$ ¹, as also shown consistently by three different methods used to reconstruct the primordial power spectrum (PPS) of curvature perturbations with *Planck* data [4]. Note however that none of these puzzling features in

¹Note that $k \sim 0.002 \text{ Mpc}^{-1}$ roughly corresponds to $\ell \sim 20$.

the *Planck* temperature power spectrum constitute statistically significant departures from a simple power-law spectrum generated within the simplest slow-roll inflationary models.

There are several theoretically well motivated mechanisms during inflation which support deviations from a simple power law for primordial fluctuations providing a better fit to the CMB temperature power spectrum. Some of these mechanisms are based on a temporary violation of the slow-roll regime for the inflaton field and include a short inflationary stage preceded by a kinetic stage [7] or by a bounce from a contracting stage [8], a string theory-motivated climbing phase prior to inflation [9], a sharp edge in the first derivative of the potential [10], a step in the potential [11], a variation in the effective speed of sound [12, 13]. Other models such as axion monodromy inflation [14] motivate periodic oscillations on a large field potential [15] which induce weak periodic oscillations in the inflaton evolution and therefore super-imposed periodic oscillations to the PPS [16] (see [17] for a review on primordial features). These features in the power spectrum are accompanied by specific templates in the bispectrum (see [18] for a review): therefore primordial features can also be searched in the bispectrum [19] or jointly in the power spectrum and bispectrum [20, 21]. At present, no inflationary model fitting these features has been found to be preferred at a statistical significant level over more standard models [4, 19].

Thanks to the sharpness of the CMB polarization transfer functions [4, 17], future CMB polarization data will help in providing complementary information to further test if these deviations from a simple power-law spectrum are statistical fluctuations or are of primordial origin. However, some of the polarization imprints of primordial features in the E-mode power spectrum could be confused with cosmic variance plus noise or could be degenerate with the physics of reionization beyond the simplest modelling of an average optical depth [22]. For primordial features fitting the $\ell \lesssim 40$ pattern in the CMB temperature power spectrum, it has been estimated that the confusion of a complex reionization phase could decrease the statistical significance in detecting the features due to a step in the inflaton potential [11] from 8 to 5 σ for a cosmic variance dominated CMB experiment [22].

Beyond the handle of better measurements of CMB polarization, the current snapshot of the PPS taken by *Planck* [4, 23] will be also further refined by future galaxy surveys as J-PAS ² [24], DESI ³ [25, 26], Euclid ⁴ [27, 28], SPHEREx ⁵ [29, 30], LSST ⁶ [31], SKA ⁷ [32] and others. Thanks to the different sensitivity of the matter power spectrum to cosmology, future galaxy surveys will be useful to break the degeneracy among cosmological parameters encoded in the CMB angular power spectra of temperature and polarization.

The main goal of this paper is to assess in a quantitative way the capability of the galaxy power spectrum expected from future surveys having an accurate determination of redshift to probe few selected examples of inflationary models with a violation of the slow-roll approximation which provide a fit to the *Planck* 2015 data improving on the Λ CDM model. In particular we restrict ourselves to DESI, Euclid and SPHEREx as a selection of future galaxy surveys which probe a sufficiently large volume with an accurate determination of redshift, but with different characteristics (see section 4).

Our paper is organized as follows. After this introduction, in section 2 we describe the

²<http://www.j-pas.org/>

³<http://desi.lbl.gov/>

⁴<http://sci.esa.int/euclid/>

⁵<http://spherex.caltech.edu/>

⁶<http://www.lsst.org/>

⁷<http://www.skatelescope.org/>

four representative inflationary models which are taken as examples for a better fit to the *Planck* 2015 data, compared with the baseline Λ CDM model. In section 3 we review the Fisher matrix approach and we describe the CMB data and galaxy surveys in section 4. In section 5 we presents our results and we conclude in section 6, comparing our findings to previous studies in the literature [33, 34].

2 Deviations from a simple power law for primordial fluctuations consistent with *Planck*

Primordial adiabatic fluctuations with a nearly Gaussian statistics and a smooth power spectrum⁸ are a generic prediction of standard - i.e. with a standard kinetic term - slow-roll single field inflationary models with Bunch-Davies vacuum. The amplitude A_s , the spectral index n_s and the running $dn_s/d\ln k$ of the power spectrum for the curvature perturbation $\mathcal{P}_{\mathcal{R}}(k)$:

$$\ln[\mathcal{P}_{\mathcal{R}}(k)] = \ln(A_s) + (n_s - 1) \ln\left(\frac{k}{k_*}\right) + \frac{1}{2} \frac{d n_s}{d \ln k} \ln^2\left(\frac{k}{k_*}\right) + \dots \quad (2.1)$$

are connected to the Hubble parameter H and the Hubble flow functions (HFF) ϵ_i during inflation:

$$A_s \approx \frac{H_*^2}{8\pi^2 \epsilon_{1*}} \quad (2.2)$$

$$n_s - 1 \approx -2\epsilon_{1*} - \epsilon_{2*} \quad (2.3)$$

$$\frac{d n_s}{d \ln k} \approx -2\epsilon_{1*}\epsilon_{2*} - \epsilon_{2*}\epsilon_{3*}, \quad (2.4)$$

where \approx denotes the lowest order in the slow-roll parameters and the pedix $*$ represents the value of the quantity at the time in which the pivot scale k_* crosses the Hubble radius during inflation ($k_* = a_* H_*$). The HFF functions are defined through an hierarchy of equations involving derivatives of the Hubble parameter, i.e. $\epsilon_{i+1} \equiv \frac{d \ln \epsilon_i}{d \ln a}$ with $\epsilon_0 \propto H^{-1}$. When slow-roll holds with $\epsilon_i \ll 1$, the running and higher terms in the expansion (2.1) are suppressed - being quadratic or higher order in the slow-roll parameters - and therefore the power spectrum is well approximated by a power-law. The extension to non-standard kinetic term introduces an additional parameter, the inflaton sound speed [35, 36], in general time-dependent with its own hierarchy of higher derivative coupled to the HFFs.

Features and/or localized bumps in the power spectra within single field inflation can occur when the slow-roll approximation breaks down with ϵ_1 and/or ϵ_2 not small. In the following we consider four well known examples of temporary violation of the slow-roll approximation and the relative analytic approximation for the resulting curvature power spectrum. In this paper we restrict ourselves to an inflaton with a standard kinetic term, since this class of models already provide a case sufficient for our purposes and hereafter we refer to the standard PPS $\mathcal{P}_{\mathcal{R},0}(k)$ as defined in eq. (2.1) with $\frac{d n_s}{d \ln k} = 0$.

⁸We define the power spectrum for a variable X as $\mathcal{P}_{\mathcal{X}}(k) \equiv k^3 |X_k|^2 / (2\pi^2)$, where X_k is the Fourier transform of X .

Table 1. Best-fit for the six standard cosmological parameters and the extra parameters [4] obtained with the BOBYQA algorithm [42] keeping fix the foreground parameters around their best-fit value for the Λ CDM case with *Planck* TT + lowP [4]. The six cosmological parameters are: the baryon physical density ω_b , the CDM physical density ω_c , the Hubble parameter H_0 , the average optical depth τ , the amplitude and tilt of the PPS, A_s and n_s . See section 2 for details on the extra parameters for MI, MII, MIII, MIV.

Parameter	Baseline	MI	II	MIII	MIV
ω_b	0.02222	0.02228	0.02227	0.02223	0.2240
ω_c	0.1198	0.1197	0.1198	0.1201	0.1184
$H_0[\text{km s}^{-1} \text{Mpc}^{-1}]$	67.31	67.40	67.32	67.18	68.01
τ	0.078	0.085	0.088	0.082	0.085
$\ln(10^{10} A_s)$	3.089	3.103	3.109	3.089	3.102
n_s	0.9655	0.9647	0.9655	0.9647	0.9723
λ_c	...	0.50
$\log_{10}(k_c \text{ Mpc})$...	-3.47
Δ	0.089
$\log_{10}(k_s \text{ Mpc})$	-3.05
\mathcal{A}_{st}	0.374	...
$\log_{10}(k_{\text{st}} \text{ Mpc})$	-3.10	...
$\ln x_{\text{st}}$	0.342	...
\mathcal{A}_{log}	0.0278
$\log_{10}(\omega_{\text{log}})$	1.51
$\phi_{\text{log}}/(2\pi)$	0.634

2.1 Model 1: An exponential cut-off on large scales with variable stiffness

As first model (hereafter MI), we analyze a power-law spectrum multiplied by an exponential cut-off, introduced in [7], parametrized as:

$$\mathcal{P}_{\mathcal{R}}(k) = \mathcal{P}_{\mathcal{R},0}(k) \left\{ 1 - \exp \left[- \left(\frac{k}{k_c} \right)^{\lambda_c} \right] \right\}. \quad (2.5)$$

Here, eq. (2.5) reproduces a suppression of the curvature power spectrum at large scales by introducing two extra parameters: the first one, k_c , selects the relevant scale where the deviation from the smooth curvature power spectrum starts, while the second parameter, λ_c , adjusts the stiffness of the suppression.

This simple parameterization is motivated by models with a kinetic stage followed by a short inflationary phase in which the onset of the slow-roll phase coincides with the time when the largest observable scales exited the Hubble radius during inflation⁹. On these largest scales, the curvature power spectrum is then strongly suppressed due to the kinetic energy of the inflaton, and so the CMB angular power spectra at the lowest multipoles. Note that the exact derivation of the PPS obtained through a matching of an initial kinetic-dominated regime with a de-Sitter stage showed that the suppression is connected to the smooth nearly scale-invariant power spectrum by oscillations [7]. However, this exact derivation leads to

⁹A change in the power spectrum at large scales might also be induced by first-order quantum gravity corrections [37].

a smaller improvement in $\Delta\chi^2$ with respect to the smooth phenomenological suppression described by eq. (2.5) [4] and therefore we choose the latter as the first representative case of this paper.

2.2 Model 2: Discontinuity in the first derivative of the potential

As a second model (hereafter MII), we consider a transition in the first derivative of the potential, which leads to a localized imprint in the PPS, at the scales where the transition occurred [10]. This specific model assumes a sharp change in the slope of the inflaton potential $V(\phi)$:

$$V(\phi) = \begin{cases} V_0 + A_+(\phi - \phi_0), & \phi \gg \phi_0 \\ V_0 + A_-(\phi - \phi_0), & \phi \ll \phi_0 \end{cases}. \quad (2.6)$$

The two different slopes of the potential lead to different asymptotic values of the curvature power spectrum, plus an oscillatory pattern in between. The curvature power spectrum can be obtained analitically under the approximation $|A_+\phi|, |A_-\phi| \ll V_0$ [10]:

$$\mathcal{P}_{\mathcal{R}}(k) = \mathcal{P}_{\mathcal{R},0}(k) \times \mathcal{D}(y, \Delta), \quad (2.7)$$

with:

$$\begin{aligned} \mathcal{D}(y, \Delta) = & 1 + \frac{9\Delta^2}{2} \left(\frac{1}{y} + \frac{1}{y^3} \right)^2 + \frac{3\Delta}{2} \left(4 + 3\Delta - \frac{3\Delta}{y^4} \right)^2 \frac{1}{y^2} \cos(2y) \\ & + 3\Delta \left(1 - \frac{1 + 3\Delta}{y^2} - \frac{3\Delta}{y^4} \right)^2 \frac{1}{y} \sin(2y), \end{aligned} \quad (2.8)$$

where $y = k/k_s$ and $\Delta = (A_+ - A_-)/A_+$. Here k_s is the scale of the transition.

2.3 Model 3: Step in the inflaton potential

We now consider a different model (hereafter MIII) with a step in the inflationary potential [11] wich predicts localized oscillations in the power spectrum. In this case the parameterization for the PPS is derived from the potential:

$$V(\phi) = \frac{1}{2}m^2\phi^2 \left[1 + c \tanh \left(\frac{\phi - \phi_0}{b} \right) \right], \quad (2.9)$$

where c is the height and d the width of the step localized at $\phi = \phi_0$. This step-like feature in the inflaton potential leads to a localized oscillatory pattern with a negligible difference in the asymptotic amplitudes of the PPS. An analytic approximation for the PPS describing the step in the potential is [38, 39]:

$$\mathcal{P}_{\mathcal{R}}(k) = \exp \left\{ \ln \mathcal{P}_{\mathcal{R},0}(k) + \mathcal{I}_0(k) + \ln [1 + \mathcal{I}_1^2(k)] \right\}, \quad (2.10)$$

where the first-order term is:

$$\mathcal{I}_0(k) = \mathcal{A}_{\text{st}} W' \left(\frac{k}{k_{\text{st}}} \right) \mathcal{D} \left(\frac{k}{k_{\text{st}} x_{\text{st}}} \right), \quad (2.11)$$

and the second-order contribution is [39]:

$$\sqrt{2}\mathcal{I}_1(k) = \frac{\pi}{2} (1 - n_s) + \mathcal{A}_{\text{st}} X' \left(\frac{k}{k_{\text{st}}} \right) \mathcal{D} \left(\frac{k}{k_{\text{st}} x_{\text{st}}} \right), \quad (2.12)$$

where k_{st} is the mode corresponding to the time of the transition and x_{st} is related to the duration of the violation of slow-roll. The window functions in eqs. (2.11) and (2.12) are:

$$W(x) = \frac{3 \sin(2x)}{2x^3} - \frac{3 \cos(2x)}{x^2} - \frac{3 \sin(2x)}{2x} \quad (2.13)$$

$$X(x) = \frac{3}{x^3} (\sin x - x \cos x)^2 ; \quad (2.14)$$

the prime in this context denotes $d/d \ln x$ and the damping envelope is:

$$\mathcal{D}(x) = \frac{x}{\sinh x} . \quad (2.15)$$

We can rewrite the full power spectrum of curvature perturbation as [38, 39]:

$$\begin{aligned} \mathcal{P}_{\mathcal{R}}(k) = \exp \Big\{ & \ln \mathcal{P}_{\mathcal{R},0}(k) \\ & + \frac{\mathcal{A}_{\text{st}} k_{\text{st}}^3}{2k^3} \left[\left(18 \frac{k}{k_{\text{st}}} - 6 \frac{k^3}{k_{\text{st}}^3} \right) \cos \left(2 \frac{k}{k_{\text{st}}} \right) + \left(15 \frac{k^2}{k_{\text{st}}^2} - 9 \right) \sin \left(2 \frac{k}{k_{\text{st}}} \right) \right] \frac{k \cosh \left(\frac{k}{k_{\text{st}} x_{\text{st}}} \right)}{k_{\text{st}} x_{\text{st}}} \\ & + \ln \left[1 + \frac{1}{2} \left(\frac{\pi}{2} (1 - n_s) - \frac{3 \mathcal{A}_{\text{st}} k_{\text{st}}^3}{k^3} \left[\frac{k}{k_{\text{st}}} \cos \left(\frac{k}{k_{\text{st}}} \right) - \sin \left(\frac{k}{k_{\text{st}}} \right) \right] \right. \right. \\ & \quad \left. \left. \cdot \left[3 \frac{k}{k_{\text{st}}} \cos \left(\frac{k}{k_{\text{st}}} \right) + \left(2 \frac{k^2}{k_{\text{st}}^2} - 3 \right) \sin \left(\frac{k}{k_{\text{st}}} \right) \right] \frac{k \cosh \left(\frac{k}{k_{\text{st}} x_{\text{st}}} \right)}{k_{\text{st}} x_{\text{st}}} \right)^2 \right] \right\} , \end{aligned} \quad (2.16)$$

where \mathcal{A}_{st} tunes the amplitude of the feature.

2.4 Model 4: Logarithmic super-imposed oscillations

As a fourth model (hereafter MIV), we study the case of logarithmic super-imposed oscillations to the PPS:

$$\mathcal{P}_{\mathcal{R}}(k) = \mathcal{P}_{\mathcal{R},0}(k) \left[1 + \mathcal{A}_{\log} \cos \left(\omega_{\log} \ln \left(\frac{k}{k_*} \right) + \phi_{\log} \right) \right] . \quad (2.17)$$

This pattern can be generated by different mechanisms. Axion monodromy inflation [14] motivates periodic oscillations on a large field inflaton potential leading to an approximated analytic PPS as in eq. (2.17) [16]. See also [40] for the most recent developments including drifting oscillations. Logarithmic super-imposed oscillations can also be generated by initial quantum states different from Bunch-Davies [41].

2.5 Current constraints from CMB

All the four models described above have been analysed in ref. [4]. In table 1 we show for each models the best-fit parameters for the standard cosmological parameters and for the extra parameters obtained with *Planck* TT + lowP [4]. We plot in figure 1 the PPS for the four representative inflationary models and the baseline Λ CDM model. None of the four models is preferred by *Planck* TT + lowP over the baseline Λ CDM model ¹⁰.

¹⁰The Bayes factors for the four models with respect to the baseline Λ CDM model are -1.4 , -0.6 , -0.3 , -1.9 [4], respectively, with the following priors [4]: $\log_{10}(k_c \text{ Mpc}) \in [-12, -3]$ and $\lambda_c \in [0, 10]$ for MI, $\log_{10}(k_s \text{ Mpc}) \in [-5, 0]$ and $\Delta \in [-0.5, 0.5]$ for MII, $\log_{10}(k_{\text{st}} \text{ Mpc}) \in [-5, 0]$, $\mathcal{A}_{\text{st}} \in [0, 2]$ and $\ln(x_{\text{st}}) \in [-1, 5]$ for MIII, $\mathcal{A}_{\log} \in [0, 0.5]$, $\log_{10}(\omega_{\log}) \in [0, 2.1]$ and $\phi_{\log} \in [0, 2\pi]$ for MIV.

For the cut-off model (MI), the best-fit for the effective scale k_c , which marks the departure from a tilted power spectrum, is found at very large scales with *Planck* 2015 data [4], i.e. $k_c \simeq 4 \times 10^{-4} \text{ Mpc}^{-1}$. The improvement in the fit for this model - $\Delta\chi^2 \approx -3.4$ for *Planck* TT + lowP [4] - is due to the lower amplitude at $\ell \lesssim 40$ for the CMB temperature power spectrum.

For the other two models, which include oscillations, the effective scale of the feature is instead of the order of 10^{-3} Mpc^{-1} . For the second model (MII) the improvement in the fit - $\Delta\chi^2 \approx -4.5$ for *Planck* TT + lowP [4] - is due either to the lower amplitude at $\ell \lesssim 40$ and to the feature at $\ell \sim 20$. The model with a step in the potential (MIII) fits much better the feature at $\ell \sim 20$ and provides $\Delta\chi^2 \approx -8.6$. Note that a low value for the quadrupole and oscillations at $\ell \sim (20 - 40)$ was also present in WMAP data [43]; however, only the precision of the *Planck* measurement in the region of the acoustic peaks has shown how the models discussed so far provide a better fit to CMB data than the simplest extended model with a negative running of the scalar spectral index.

The model with logarithmic oscillations (MIV) provides $\Delta\chi^2 \approx -10.8$ for *Planck* TT + lowP [4], which is mainly driven by fitting outliers from the best-fit ΛCDM at multipoles $\ell \gtrsim 100$.

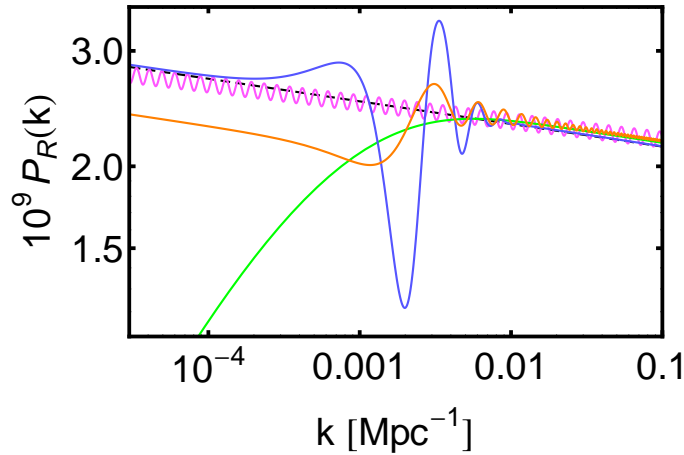


Figure 1. We show the PPS for a power-law spectrum (dashed black line), for MI (green solid line), for MII (orange solid line), MIII (blue solid line) and MIV (magenta solid line). The parameters for the different models are listed in table 1.

3 Combined Forecast for CMB and LSS

We use the Fisher matrix technique [44] for our science forecasts. In this context the Fisher matrix technique approximates the logarithm of the likelihood as a multivariate Gaussian in the cosmological parameters $\{\theta_i\}$ around a maximum, which we will denote as $\{\bar{\theta}_i\}$. The logarithm of the likelihood can be expanded as a Taylor series and the Fisher matrix can be approximated as the second derivative around the peak:

$$F_{ij} = - \left\langle \frac{\partial^2 \ln \mathcal{L}}{\partial \theta_i \partial \theta_j} \right\rangle = - \frac{\partial^2 \ln \mathcal{L}}{\partial \theta_i \partial \theta_j} \Big|_{\bar{\theta}}. \quad (3.1)$$

The resulting covariance of the parameters is given by the inverse of the Fisher matrix F_{ij}^{-1} as:

$$\text{Cov}(\theta_i, \theta_j) \geq [F^{-1}]_{ij} , \quad (3.2)$$

where we perform the inversion of the matrix before.

In the next two subsections we describe the CMB and LSS likelihoods and the corresponding Fisher matrices [45], which will be added to obtain our combined results.

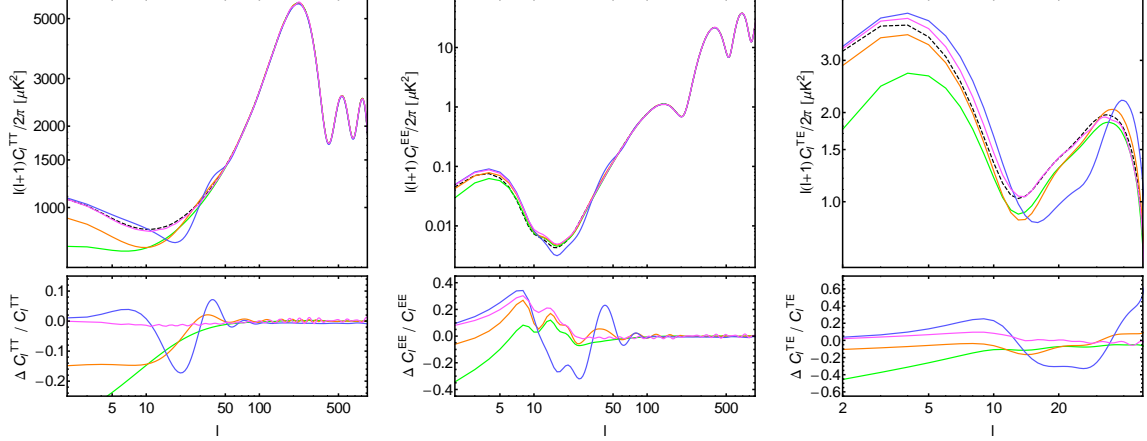


Figure 2. Lensed angular power spectra TT (left panel), TE (middle panel), EE (right panel) for the baseline Λ CDM model (black dashed line), for MI (green solid line), for MII (orange solid line), MIII (blue solid line) and MIV (magenta solid line). In the bottom panels we display the corresponding relative differences of the models with respect to the baseline Λ CDM model.

3.1 Fisher matrix for CMB

We consider as CMB observables the lensed TT, EE and TE angular power spectra with the best-fit parameters showed in table 1. In figure 2 we show these angular power spectra for the four best-fits and the relative differences with respect to the baseline Λ CDM model.

To compute the Fisher matrix for the polarized CMB angular power spectra [46–50] we use eq. (3.2) with observables being the autocorrelators of temperature and E-mode polarization, and their cross-correlation¹¹. We consider the lensed polarized CMB angular spectra, although not taking into account the CMB deflection angle information as a separate observable. The covariance matrix for the observables is given by:

$$F_{ij}^{\text{CMB}} = \sum_{\ell} \sum_{X,Y} \frac{\partial C_{\ell}^X}{\partial \theta_i} (\text{Cov}_{\ell})_{XY}^{-1} \frac{\partial C_{\ell}^Y}{\partial \theta_j} , \quad (3.3)$$

where we consider $X, Y \in (\text{TT}, \text{EE}, \text{TE})$ and the matrix Cov_{ℓ} is the symmetric angular power spectrum covariance matrix at the ℓ -th multipole:

$$\text{Cov}_{\ell} = \frac{2}{(2\ell+1)f_{\text{sky}}} \begin{bmatrix} (\bar{C}_{\ell}^{\text{TT}})^2 & (\bar{C}_{\ell}^{\text{TE}})^2 & \bar{C}_{\ell}^{\text{TT}}\bar{C}_{\ell}^{\text{TE}} \\ (\bar{C}_{\ell}^{\text{TE}})^2 & (\bar{C}_{\ell}^{\text{EE}})^2 & \bar{C}_{\ell}^{\text{EE}}\bar{C}_{\ell}^{\text{TE}} \\ \bar{C}_{\ell}^{\text{TT}}\bar{C}_{\ell}^{\text{TE}} & \bar{C}_{\ell}^{\text{EE}}\bar{C}_{\ell}^{\text{TE}} & ((\bar{C}_{\ell}^{\text{TE}})^2 + \bar{C}_{\ell}^{\text{TT}}\bar{C}_{\ell}^{\text{EE}})/2 \end{bmatrix} , \quad (3.4)$$

¹¹In this paper we restrict ourselves to TT, EE, TE, although extensions of the models considered here exhibit a non-trivial tensor-to-scalar ratio if the energy-scale of inflation is sufficiently large [51].

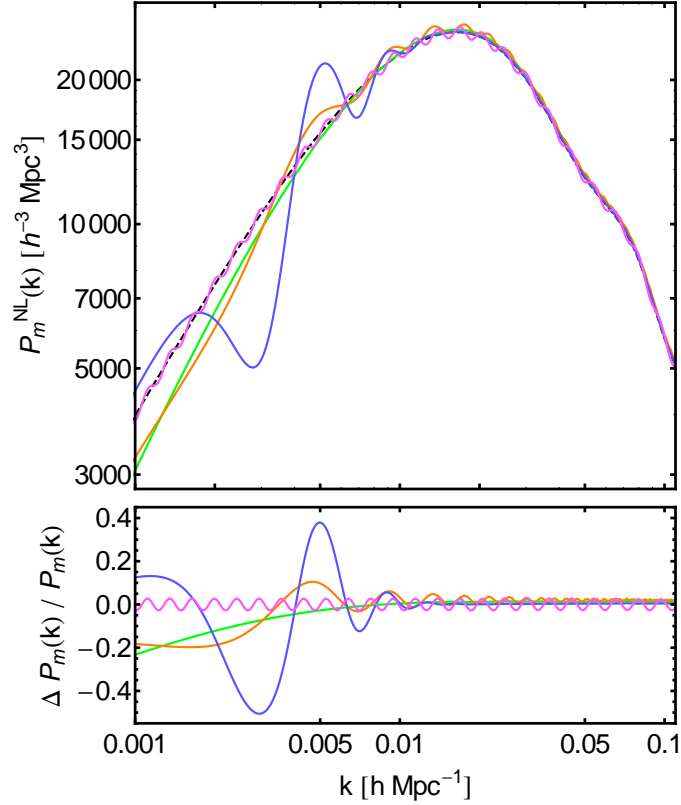


Figure 3. In the top panel we show the non-linear matter power spectrum for Λ CDM (dashed black line), for MI (green solid line), for MII (orange solid line), MIII (blue solid line) and MIV (magenta solid line). In the bottom panel we display the corresponding relative differences of the models with respect to the baseline Λ CDM model.

where $\bar{C}_\ell^X = C_\ell^X + N_\ell^X$ is the sum of the signal and the noise, with $N_\ell^{\text{TE}} = 0$. Here $N_\ell^X = w_X^{-1} b_\ell^{-2}$ is the isotropic noise convolved with the instrument beam, b_ℓ^2 is the Gaussian beam window function, with $b_\ell = e^{-\ell(\ell+1)\theta_{\text{FWHM}}^2/16 \ln 2}$; θ_{FWHM} is the full width half maximum (FWHM) of the beam in radians; w_{TT} and w_{EE} are the inverse square of the detector noise level on a steradian patch for temperature and polarization, respectively. For multiple frequency channels, $w_X b_\ell^2$ is replaced by the inverse noise-weighted sum over channels. Eq. (3.4) includes sampling variance for $f_{\text{sky}} < 1$ which accounts for the loss of information due to partial sky coverage. We compute the CMB angular power spectra in eqs. 3.3 and 3.4 using a modified version of the publicly available Einstein-Boltzmann code CAMB¹² [52, 53] in order to calculate C_ℓ at each multipoles.

We consider a $\mathbf{F}_{ij}^{\text{CMB}}$ which represents the CMB measurements at the timescales of the galaxy surveys analyzed here. In this paper we restrict ourselves to noise sensitivity and angular resolution to characterize the uncertainties in the CMB temperature and polarization spectra, although we know that the accuracy of CMB anisotropies measurements are not governed only by noise sensitivity and angular resolution, but limited in temperature at high multipoles by foreground residuals/secondary anisotropies and at low multipoles in polarization by the Galactic emission. Since the time scales of the surveys are different, and not

¹²<http://camb.info/>

only the *Planck* final data in temperature and polarization, but possibly other measurements of CMB E-mode polarization on a large fraction of the sky, such as from AdvACTpol [54], CLASS [55], LSPE [56], will be available, we consider two settings, one more conservative (hereafter CMB-1) and another with better sensitivity and angular resolution (CMB-2).

We therefore consider the *Planck* 143 GHz channel as CMB-1 and the inverse noise weighted combination of the *Planck* 70, 100, 143 and 217 GHz channels as CMB-2. We consider updated full mission sensitivities and angular resolution as given in [2]. We consider $f_{\text{sky}} = 0.75$, a sum up to $\ell_{\text{max}} = 2500$ in eq. (3.3).

3.2 Fisher matrix for spectroscopic galaxy surveys

We consider the galaxy clustering as observable for the Fisher LSS forecast in eq. (3.2). The simplest model for the observed galaxy power spectrum assumes a linear and scale-independent galaxy bias, with redshift space distortions due to small peculiar velocities not associated to the Hubble flow [57] given by:

$$P_g(\mathbf{k}, z) = b(z)^2 [1 + \beta(k, z)\mu^2]^2 P_m(k, z), \quad (3.5)$$

where b is the bias, which maps the mass field into the galaxy density one, $\beta \equiv f/b$ with $f \equiv d \ln D / d \ln a$ is the growth rate, μ is the angle to the line of sight and P_m represents the dark matter power spectrum in real space. For a Poisson sampled density field, we obtain in addition a constant shot-noise contribution to the power due to the finite number of galaxies per bin $P_{\text{shot}}(z)$:

$$P_{\text{obs}}(\mathbf{k}, z) = P_g(\mathbf{k}, z) + P_{\text{shot}}(z). \quad (3.6)$$

In redshift space, the observed galaxy power spectrum can be modelled by including inaccuracies in the observed redshifts as [58]:

$$\tilde{P}_{\text{obs}}(\mathbf{k}, z) = P_{\text{obs}}(\mathbf{k}, z) e^{-k^2 \mu^2 \sigma_r^2}, \quad (3.7)$$

where $\sigma_r \simeq \bar{\sigma}_z(1+z)c/H(z)$ are the spectrometric redshift errors. We did not take into account geometrical distortions induced from the assumption of a fiducial cosmology in the computation of distances since negligible [59].

Under the assumption that the density field has a Gaussian statistics and uncorrelated Fourier modes, the Fisher matrix for the broadband power spectrum eq. (3.7), for a given redshift bin with \bar{z} as centroid value, is [60]:

$$F_{ij}^{\text{gg}}(\bar{z}) = \int_{k_{\text{min}}}^{k_{\text{max}}} \frac{d^3 \mathbf{k}}{2(2\pi)^3} \frac{\partial \ln \tilde{P}_{\text{obs}}(\mathbf{k}|\bar{z})}{\partial \theta_i} \Big|_{\bar{\theta}} \frac{\partial \ln \tilde{P}_{\text{obs}}(\mathbf{k}|\bar{z})}{\partial \theta_j} \Big|_{\bar{\theta}} V_{\text{eff}}(\mathbf{k}|\bar{z}) \quad (3.8)$$

$$= \int_{k_{\text{min}}}^{k_{\text{max}}} \frac{k^2 dk}{(2\pi)^2} \int_0^1 d\mu \frac{\partial \ln \tilde{P}_{\text{obs}}(k, \mu|\bar{z})}{\partial \theta_i} \Big|_{\bar{\theta}} \frac{\partial \ln \tilde{P}_{\text{obs}}(k, \mu|\bar{z})}{\partial \theta_j} \Big|_{\bar{\theta}} V_{\text{eff}}(k, \mu|\bar{z}), \quad (3.9)$$

where the effective volume of the survey in Fourier space, which determines the mode counts, is [61]:

$$V_{\text{eff}}(k, \mu|\bar{z}) = \int_{k_{\text{min}}}^{k_{\text{max}}} \frac{d^3 \mathbf{r}}{(2\pi)^3} \left[\frac{\bar{n}_g(\bar{z}) \tilde{P}_{\text{obs}}(k, \mu|\bar{z})}{\bar{n}_g(\bar{z}) \tilde{P}_{\text{obs}}(k, \mu|\bar{z}) + 1} \right]^2 \quad (3.10)$$

$$\simeq \left[\frac{\bar{n}_g(\bar{z}) \tilde{P}_{\text{obs}}(k, \mu|\bar{z})}{\bar{n}_g(\bar{z}) \tilde{P}_{\text{obs}}(k, \mu|\bar{z}) + 1} \right]^2 V_{\text{surv}}(\bar{z}), \quad (3.11)$$

which depends on the geometrical volume of the survey, V_{surv} , and on the average number density, \bar{n}_g , of tracers in a specific redshift bin. We consider the information up to the quasi non-linear scales, i.e. $k \leq 0.1 \text{ h Mpc}^{-1}$ in all redshift bins. In these equations k_{min} is set by the survey volume, i.e. $k_{\text{min}}(\bar{z}) = 2\pi/\sqrt[3]{V_{\text{surv}}(\bar{z})}$. We consider $k \geq k_{\text{min}}(\bar{z})$ with a linear binning scheme, adopting the minimum $\Delta k = 1.4/\sqrt[3]{V_{\text{surv}}(\bar{z})}$ for which the correlation between different bins can be neglected [62]. Eq. (3.8) can be therefore rewritten as a binned sum over k and μ :

$$\mathbf{F}_{ij}^{gg}(\bar{z}) = \sum_{k,\mu} \frac{\partial \ln \tilde{P}_{\text{obs}}(k, \mu|\bar{z})}{\partial \theta_i} \Big|_{\bar{\theta}} [\text{Cov}_{\mathbf{k}}(\bar{z})]^{-1} \frac{\partial \ln \tilde{P}_{\text{obs}}(k, \mu|\bar{z})}{\partial \theta_j} \Big|_{\bar{\theta}}, \quad (3.12)$$

where

$$\text{Cov}_{\mathbf{k}}(\bar{z}) = \frac{(2\pi)^2}{k^2 \Delta k \Delta \mu} \frac{1}{V_{\text{eff}}(k, \mu|\bar{z})}. \quad (3.13)$$

We consider 10 bins in μ between 0 and 1. The derivative in eq. (3.12) is [58]:

$$\frac{d \ln \tilde{P}_{\text{obs}}(k, \mu|\bar{z})}{d \theta_i} \simeq \frac{\partial \ln P_m(k|\bar{z})}{\partial \theta_i} + \frac{2\mu^2}{1 + \beta(k|\bar{z})\mu^2} \frac{\partial \beta(k|\bar{z})}{\partial \theta_i} \quad (3.14)$$

$$+ \frac{2}{b(\bar{z})(1 + \beta(k|\bar{z})\mu^2)} \frac{\partial b(\bar{z})}{\partial \theta_i} + \frac{1}{P_{\text{obs}}(k, \mu|\bar{z})} \frac{\partial P_{\text{shot}}(\bar{z})}{\partial \theta_i} - k^2 \mu^2 \frac{\partial \sigma_{\mathbf{r}}^2}{\partial \theta_i}. \quad (3.15)$$

We compute the Fisher matrix using CAMB to calculate the exact linear matter power spectrum for each bin and Halofit [63] to include its non-linear evolution on small scales. The derivatives in eq. (3.8), and consistently in eq. (3.3), are calculated numerically with the symmetric difference quotient:

$$\frac{\partial \ln f(\mathbf{k}|\bar{\theta})}{\partial \theta_i} \simeq \frac{f(\mathbf{k}|\theta_i + \Delta_i) - f(\mathbf{k}|\theta_i - \Delta_i)}{2\Delta_i f(\mathbf{k}|\bar{\theta})}, \quad (3.16)$$

where we choose the stepsize Δ_i in order to reproduce the 68 % confidence limit of the parameters θ_i . We have checked that the results are stable with respect to changes in the stepsize.

We consider the array of independent parameters θ made by three subgroups: the cosmological parameters $\theta_0 = \{\Omega_c, \Omega_b, h_0, \tau, n_s, \ln(10^{10} A_s)\}$, the extra parameters which describe the parametrization of the primordial power spectrum θ_{ext} and the nuisance parameters $\theta_{\text{nui}} = \{b, P_{\text{shot}}, \sigma_{\mathbf{r}}^2\}$. In this analysis we marginalize over θ_{nui} .

4 A selection of future LSS catalogs

In the coming years, an enormous effort will be put in the realization of large galaxy surveys having the primary goal of determining the main cosmological parameters exploiting the information hidden in the clustering properties. The power of a survey is based on its capability of providing the most accurate positions and redshifts (corresponding to distances, when a cosmological model is assumed) for the largest number of well-classified objects, distributed over the widest possible volumes. Different strategies have been designed to optimize the scientific return of a galaxy surveys maintaining the request in terms of observational time under control.

In this section we describe the three spectroscopic projects used in the following section for our forecasts. They are different examples of future LSS surveys having a wide sky coverage: DESI is an example of ground-based survey following the multi-tracer approach; Euclid is a spectroscopic survey from space observing mostly $H\alpha$ emitting galaxies at relatively high redshifts ($0.9 < z < 1.8$) with high redshift accuracy; SPHEREx is a proposed space mission covering a very large sky area, but extending to smaller redshifts ($z \leq 1$) and having larger redshift errors.

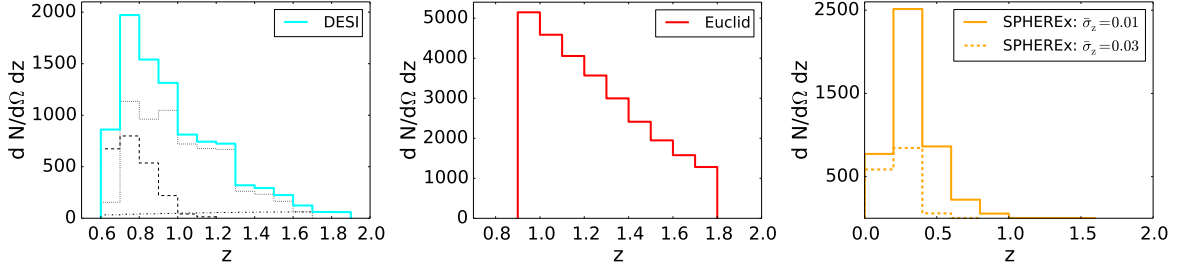


Figure 4. Number density of objects, per unit of redshift bin Δz and per square degree, used for the analysis. In the left panel we show the different tracers for DESI: LRGs (dashed), ELGs (dotted), QSOs (dot-dashed) and the total population (cyan) with a redshift bin $\Delta z = 0.1$. In the central panel we show the ELGs population expected with Euclid with a redshift bin $\Delta z = 0.1$. In the right panel we show two galaxy populations obtained for SPHEREx by considering different redshift uncertainty: the dashed (solid) line represent the observed objects considering a redshift uncertainty $\bar{\sigma}_z \sim 0.003$ (0.01) with a redshift bin $\Delta z = 0.2$.

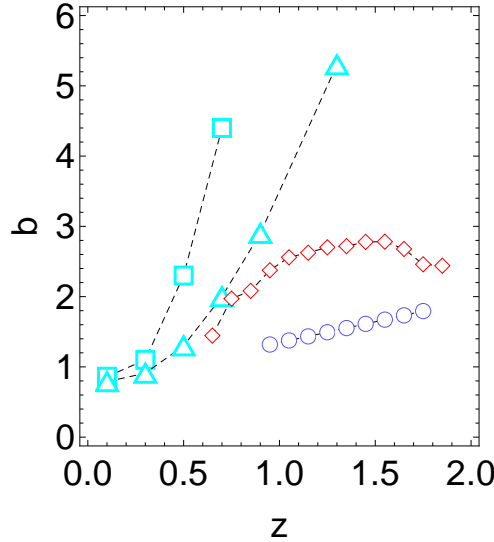


Figure 5. We show the redshift evolution of the linear bias for each of the surveys considered: red diamonds for DESI, blue circles for Euclid, cyan triangles (squares) for SPHEREx with $\bar{\sigma}_z \sim 0.01$ ($\bar{\sigma}_z \sim 0.003$).

4.1 Dark Energy Spectroscopic Instrument (DESI)

The DESI ground-based experiment [25] is expected to start observations in 2018 and to complete in 4 years a 14000 deg² redshift survey of galaxies and quasars. DESI will observe luminous red galaxies (LRGs) up to $z = 1.0$, it will target bright [OII] emission line galaxies (ELGs) up to $z = 1.7$ and quasars (QSOs) up to $z < 2.1$. DESI will also obtain a sample of bright galaxies at smaller redshifts ($0.05 < z < 0.4$) and one of higher-redshift ($2.1 < z < 3.5$) quasars looking for the Lyman- α forest absorption features in their spectra. In our analysis we use for DESI the specifications from ref. [26] (see in particular their table 2.3 and table 3.1). In particular we consider a combined galaxy clustering information for different tracers observed by DESI. In more detail we use a simplified picture in which we assume that the different populations of LRGs, ELGs and QSOs are contributing to an effective unique population, covering the redshift range between $z = 0.6$ and 1.9 , and having an effective bias given by [64]:

$$b_{\text{eff}}(z) = \frac{\bar{n}_{\text{LRG}}(z)b_{\text{LRG}}(z) + \bar{n}_{\text{ELG}}(z)b_{\text{ELG}}(z) + \bar{n}_{\text{QSO}}(z)b_{\text{QSO}}(z)}{\bar{n}_{\text{LRG}}(z) + \bar{n}_{\text{ELG}}(z) + \bar{n}_{\text{QSO}}(z)}, \quad (4.1)$$

where we assume:

$$b_{\text{LRG}}(z) = 1.7 D(0)/D(z) \quad (4.2)$$

$$b_{\text{ELG}}(z) = 0.84 D(0)/D(z) \quad (4.3)$$

$$b_{\text{QSO}}(z) = 1.34 D(0)/D(z). \quad (4.4)$$

This description is a good approximation of the exact multi-tracers approach in the limit of independent tracers [64]. For this purpose, we have also reduced the number of objects in the total sample as in [64] to include the effects of the target selection done to have a good redshift definition and to avoid confusion between different tracers and with other astrophysical objects (see the left panel of figure 4). The resulting effective bias is shown in figure 5. As error for the DESI spectroscopic redshift we use $\bar{\sigma}_z \sim 0.001$ [26]. As a reference, for DESI we obtain k_{min} ranging between $(2.42 - 3.17) \times 10^{-3} \text{ h Mpc}^{-1}$ for the different redshift bins here considered.

4.2 Euclid

The European Space Agency (ESA) Cosmic Vision mission Euclid [27] is scheduled to be launched in 2020, with the goal of characterising the dark sector of our Universe. This will be done mostly measuring the cosmic shear in a photometric surveys of billions of galaxies and the galaxy clustering in a spectroscopic survey of tens of millions of H α emitting galaxies. In this paper we will focus on the wide spectroscopic survey, which will cover an area of 15000 deg².

According to the updated predictions obtained by [65], the Euclid wide single-grism survey will reach a flux limit $F_{\text{H}\alpha} > 2 \times 10^{-16} \text{ erg cm}^{-2} \text{ s}^{-1}$ and will cover a redshift range $0.9 < z < 1.8$. With these specifications and assuming a completeness of 70 %, the expected density number of H α emitters is about 4000 objects/deg², the redshift distribution of which (taken from table 3 of ref. [65]) is shown in the central panel of figure 4. We can safely assume that the galaxy sample is composed by a single tracer, ELGs, and then assume that the bias follows eq. (4.3). Finally we adopt as redshift accuracy $\bar{\sigma}_z \sim 0.001$ [28]. As a reference, we obtain k_{min} in a range $(2.38 - 2.70) \times 10^{-3} \text{ h Mpc}^{-1}$ in the different redshift bins.

4.3 Spectro-Photometer for the History of the Universe, Epoch of Reionization, and Ices Explorer (SPHEREx)

SPHEREx [29, 30] is a NASA proposed small explorer satellite having the goal of providing the first near-infrared spectro-photometric image of the complete sky, thanks to its coverage of 40000 deg^2 in the wavelength range $0.75 < \lambda \text{ } \mu\text{m}^{-1} < 4.8$.

SPHEREx will collect spectra of galaxies at $z < 1$, covering the redshift range for clustering studies that are not covered by the Euclid spectroscopic survey. Moreover it will observe high-redshift quasars in its deep fields. In our analysis we will consider only the galaxy sample, assuming that the fraction of sky usable for clustering studies is 75 % of the whilw sky, in strict analogy to what is done in CMB analyses.

When deriving the parameters for the ΛCDM and ΛCDM plus running models we consider two different configurations for SPHEREx ¹³, with $\bar{\sigma}_z \sim 0.01$ and $\bar{\sigma}_z \sim 0.003$; however, we will restrict ourselves only to $\bar{\sigma}_z \sim 0.01$ as the best configuration when forecasting the parameters for the three parametrized non-standard PPS considered in this paper. The adopted bias is shown in figure 5. As a reference, for SPHEREx we obtain k_{min} in the range $(1.0 \div 5.1) \times 10^{-3} \text{ h Mpc}^{-1}$ [$(1.87 - 5.06) \times 10^{-3} \text{ h Mpc}^{-1}$] for $\bar{\sigma}_z \sim 0.01$ ($\bar{\sigma}_z \sim 0.003$).

5 Results and Discussions

We now discuss the uncertainties in the cosmological parameters obtained as result of our combined CMB and LSS Fisher approach.

For the ΛCDM model the uncertainties in the cosmological parameters are reported in table 5. Our results for the uncertainties from CMB and LSS are broadly consistent with the previous ones in the literature [34, 66]. We need however to bear in mind that different assumptions for CMB in combination with Euclid were considered in ref. [34] and ref. [66].

Table 2. Marginalized 68 % uncertainties for the cosmological parameters in the ΛCDM model from our LSS Fisher approach. The two results in the parentheses include the constraints obtained in combination with the CMB Fisher matrix for the two configurations (CMB-1 and CMB-2, respectively). We do not list the margined error for τ which does not benefit from the inclusion of LSS.

	DESI	Euclid	SPHEREx ($\bar{\sigma}_z = 0.003$)	SPHEREx ($\bar{\sigma}_z = 0.01$)
$10^3 \sigma(\Omega_c)$	9.1 (3.3/3.2)	7.1 (0.87/0.74)	17.0 (3.4/3.1)	9.3 (2.4/0.2.3)
$10^3 \sigma(\Omega_b)$	4.3 (0.34/0.32)	3.1 (0.21/0.19)	5.0 (0.34/0.31)	3.0 (0.27/0.25)
$\sigma(H_0)$	5.2 (0.27/0.25)	3.3 (0.080/0.061)	3.5 (0.27/0.25)	2.3 (0.20/0.19)
$10^2 \sigma(n_s)$	7.6 (0.26/0.24)	5.0 (0.24/0.23)	8.2 (0.25/0.23)	5.2 (0.24/0.22)
$10^2 \sigma(\ln(10^{10} A_s))$	29.6 (0.83/0.74)	22.6 (0.68/0.63)	39.9 (0.36/0.33)	21.6 (0.19/0.18)

We have also analyzed the case in which the dependence in the wavelength of the spectral index is allowed to vary, by fixing the fiducial model to $(n_s, dn_s/d \ln k) = (0.9655, 0.0)$. We obtain the following uncertainties $(\sigma(n_s), \sigma(dn_s/d \ln k))$: (0.0026, 0.0049) for DESI, (0.0025, 0.0044) for Euclid, (0.026, 0.0047)/(0.024, 0.0044) for SPHEREx with $\bar{\sigma}_z = 0.003/0.01$, when the CMB-1 Fisher information for the more conservative configuration is added. When combining the Fisher information for the second CMB configuration with the LSS one, the errors are

¹³We wish to thank Olivier Doré and Roland de Putter for making available the SPHEREx specifications to us.

slightly decreased as it can be seen in figure 6. Being $dn_s/d\ln k = -0.003 \pm 0.007$ the current *Planck* measurement on the running [4, 23], the parameter space with $dn_s/d\ln k$ exceeding the standard slow-roll predictions $\approx (n_s - 1)^2$ will be further probed by future galaxy surveys.

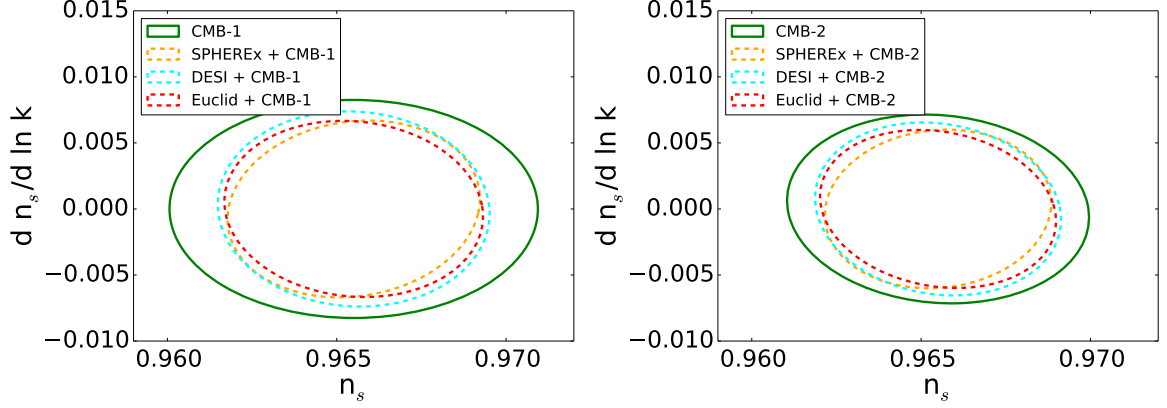


Figure 6. CMB and LSS combined constraints on $(n_s, dn_s/d\ln k)$. Different lines refer to CMB only (solid green), DESI (dashed cyan), Euclid (dashed red) and SPHEREx (dashed orange). The configuration CMB-1 (CMB-2) is considered in the left (right) panel.

We now discuss our results for the four inflationary models considered. The effective very large scale of MI obtained as a best-fit for *Planck* 2015 [4] is a challenge for the future galaxy surveys here considered (see figure 7). Such a modification on large scales seems a better target for high-sensitivity CMB polarization experiments covering a large fraction of the sky, such as *Planck*, AdvACTpol [54], CLASS [55], LSPE [56], which will provide an improved measurement of the E-mode polarization on large scales. Note that the same type of suppression of this model has been previously studied in [33]: however, the fiducial cosmological model in ref. [33] has been taken with $k_c = 9.5 \times 10^{-4} \text{ Mpc}^{-1}$, i.e. a wavenumber which is almost three times larger than the one suggested by the latest *Planck* data, and with a much steeper cut-off, i.e. $\lambda_c = 3$. The parametrized suppression of PPS chosen in [33] would be therefore a much easier target for future galaxy surveys.

The model MII, with a discontinuity in the first derivative of the potential [10], has also two parameters as the first model, but the resulting power spectrum has super-imposed oscillations accompanying the change in the amplitude of the PPS. These oscillations are non-zero at scales smaller than the change in amplitude and can be therefore a target for future galaxy surveys. Whereas CMB is sensitive to the preferred scale of the model, the matter power spectrum from galaxy surveys is more sensitive to the change in the amplitude of the power spectrum: for this model the complementarity of CMB and LSS is quite striking. As from figure 8, the scale of the feature would be probed at high statistical significance. Also in this case, a previous study [34] considered the capability of Euclid when combined with *Planck* to discriminate this model for different values of the parameters. However, in [34] a comoving scale $k_s = 6.8 \times 10^{-2} \text{ Mpc}^{-1}$, i.e. 8 times larger than the one suggested by *Planck* 2015 data and used here, was considered. Again, such a choice would enhance the possibility of detecting the feature either in CMB and LSS.

The model with a step in the potential (MIII) benefits from the addition of LSS, as it can be seen from figure 9. In this case the power spectrum of galaxy surveys is sensitive to either the amplitude and the width of the ringing features in the primordial fluctuations;

again, the scale of the feature would be probed at high statistical significance.

For the fourth model considered, CMB and LSS can probe the amplitude of periodic oscillations at high statistical significance: we obtain $\mathcal{A}_{\log} = 0.0278 \pm 0.0030$ ($\mathcal{A}_{\log} = 0.0278 \pm 0.0028$) at 68 % for CMB-1 (CMB-2) combined with Euclid. This parameterization was also studied in [34] but considering a different best-fit with a smaller amplitude and a frequency of $\omega_{\log} \sim 10$. Even if the constraint from CMB only in [34] is tighter than the one we find, the improvement from CMB and Euclid in [34] is in agreement with our finding. We also checked that our fiducial frequency, $\omega_{\log} \sim 32$, does not disappear in ℓ -space due the acoustic transfer function.

We stress that we have considered discrete bins linearly spaced for $P(k)$ with the minimum width (for every redshift slice) such as a diagonal covariance matrix is a good approximation [62]. We believe that this setting is more conservative than considering a continuous $P(k)$ in the galaxy likelihood evaluation, given three of the considered fiducial models have super-imposed oscillations. If we were considering a continuous $P(k)$, there would be no considerable changes for MI, but we would obtain tighter constraints for the other three models.

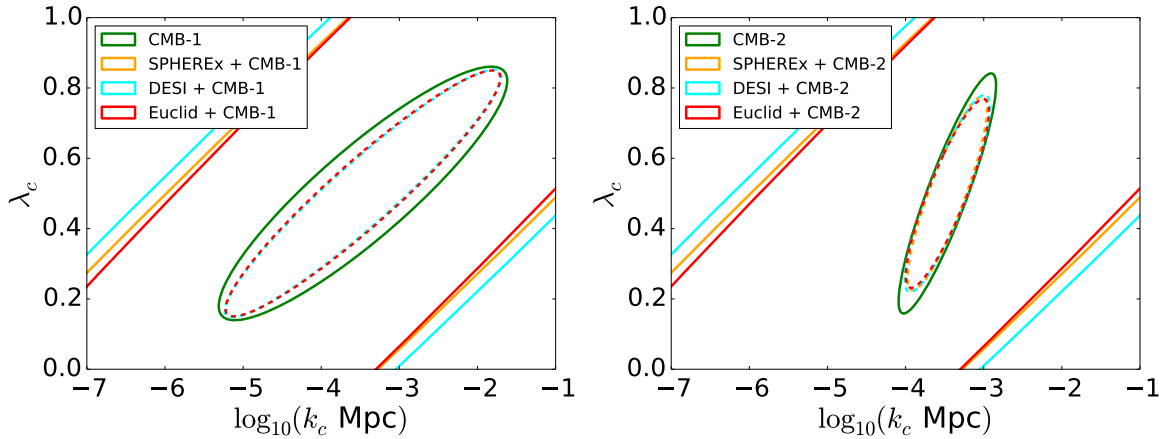


Figure 7. Marginalized 2D 68 % CL contours for the parameters $(\log_{10}(k_c \text{ Mpc}), \lambda_c)$ of MI for CMB only (solid green), DESI (solid cyan), Euclid (solid red), and SPHEREx (solid orange). The dashed contours represent the 2D 68 % CL CMB and LSS combined results. The configuration CMB-1 (CMB-2) is considered in the left (right) panel.

6 Conclusions

In this paper we have studied the complementarity between the matter power spectrum from future galaxy surveys which have an accurate determination of redshift and cover a wide volume, such as DESI, Euclid and SPHEREx, and the one from the measurements of CMB anisotropies in temperature and polarization to help in characterizing primordial features in the PPS. We have restricted ourselves to models predicting features which improve the fit to *Planck* 2015 temperature data with respect to the simplest power-law spectrum, although not at a statistical significant level.

By considering four representative deviations from a simple power-law PPS and including CMB uncertainties compatible with future measurements, we have shown that any of the surveys considered here with either a wide sky coverage and an accurate determination of redshift will be useful to decrease significantly the degeneracy among the cosmological

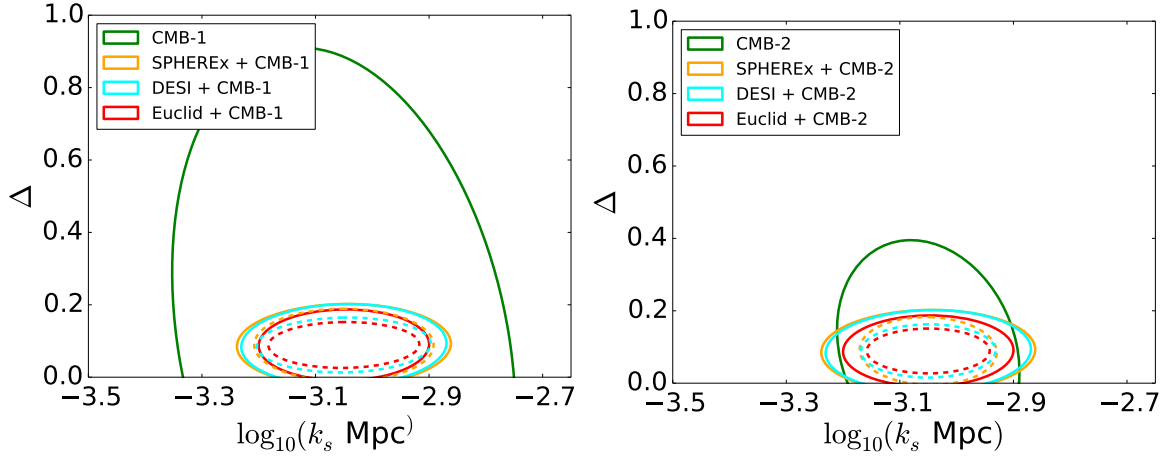


Figure 8. Marginalized 2D 68 % CL contours for the parameters $(\log_{10}(k_s \text{ Mpc}), \Delta)$ of MII for CMB only (green), DESI (solid cyan), Euclid (solid red), and SPHEREx (solid orange). The dashed contours represent the 2D 68 % CL CMB and LSS combined results. The configuration CMB-1 (CMB-2) is considered in the left (right) panel.

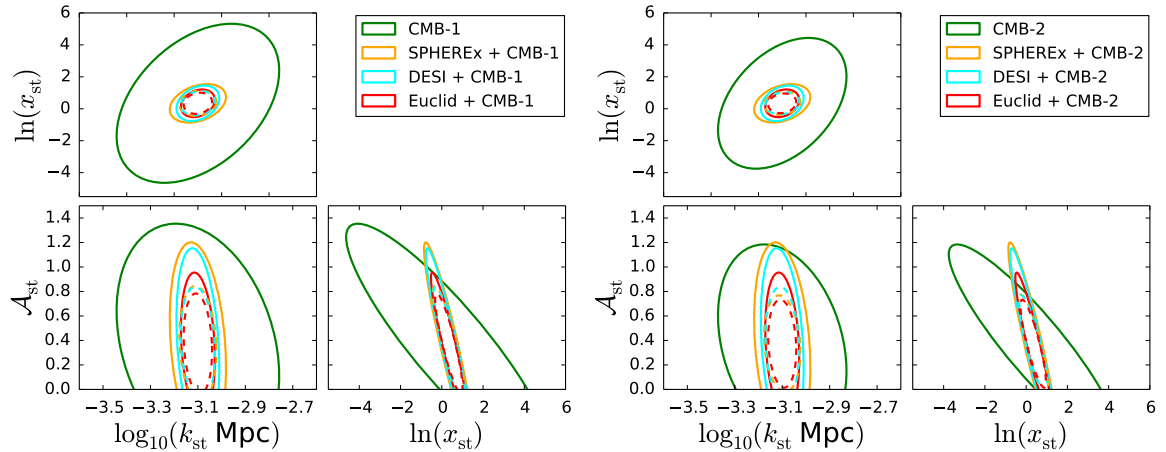


Figure 9. Triangle plot with marginalized 2D 68 % CL contours for the parameters $\mathcal{A}_{\text{st}}, \log_{10}(k_{\text{st}} \text{ Mpc}), \ln(x_{\text{st}})$ of MIII for CMB only (solid green), DESI (solid cyan), Euclid (solid red), and SPHEREx (solid orange). The dashed contours represent the 2D 68 % CL CMB and LSS combined results. The configuration CMB-1 (CMB-2) is considered in the left (right) panel.

and the features parameters. Among the four surveys considered, Euclid is the one which performs better in general for the four models studied here, even without considering the complementary information of its photometric survey.

The synergy with future galaxy surveys was also explored in previous works [33, 34]. With respect to these works, our study has compared different galaxy surveys with the most updated specifications and has considered cosmological models which lead to an improved χ^2 with respect to the simplest Λ CDM model, with the most recent data [2, 4, 67]. Instead, previous works such as Gibelyou et al. [33], in which the model with an exponential cut-off was studied, and Huang et al. [34], which considered the sharp edge in the first derivative of the potential, have adopted fiducial models with features in the PPS at comoving scales

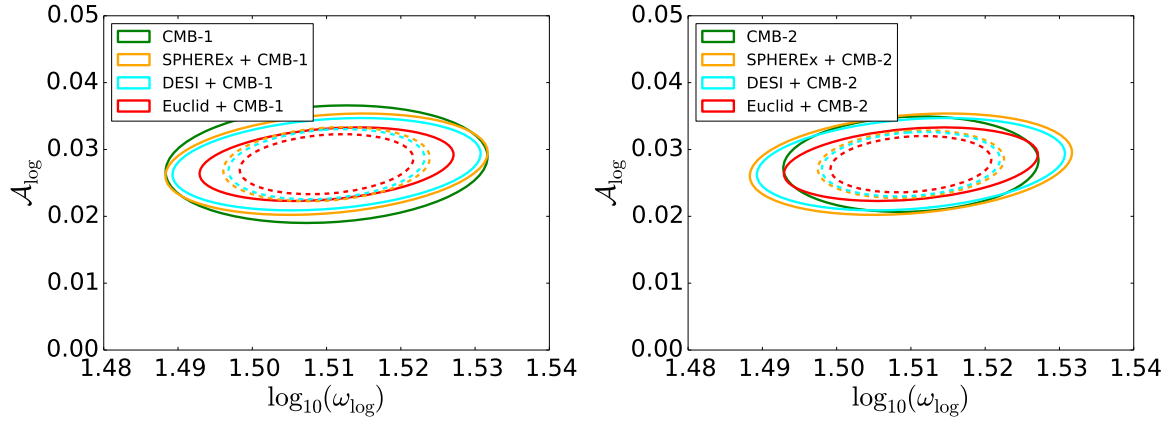


Figure 10. Marginalized 2D 68 % CL contours for the parameters $(\log_{10}(\omega_{\log}), A_{\log})$ of MIV for CMB only (green), DESI (solid cyan), Euclid (solid red), and SPHEREx (solid orange). The dashed contours represent the 2D 68 % CL CMB and LSS combined results. The configuration CMB-1 (CMB-2) is considered in the left (right) panel.

smaller than what current data seem to indicate. By choosing smaller comoving scales for the features, MI and MII could be more easily distinguished from a standard Λ CDM model, as the analysis of the fourth model explicitly shows.

Although not all (realistic and systematics) uncertainties have been taken into account in our forecasts, we have conservatively limited ourselves to the CMB angular power spectra of temperature and polarization fluctuations and to the power spectrum of galaxies from future surveys with an accurate determination of redshifts. We therefore believe that we can be optimistic even in probing features at large scales in the PPS for different reasons. In the first instance, other surveys as LSST [31] (photometric) and SKA [32] (radio) will access even larger volumes than the ones considered here. This aspect is particularly important since the features for three of the four models studied here seem effectively located at scales which are at the edge of those probed by DESI, Euclid and SPHEREx. Secondly, the deviations from a simple power law of primordial perturbations studied here can be accompanied by imprints in the CMB and/or galaxy shear, as well as in the CMB and/or galaxy bispectrum; these imprints in higher-order correlation functions can add to the ones we have considered here to further test primordial features. We hope to include some of these effects in our analysis elsewhere. Finally, future CMB space missions [68–70] will provide a final cosmic variance limited measurement of the E -mode polarization which will be crucial in discriminating a primordial origin of the features at $\ell \lesssim 40$ in the temperature power spectrum from a statistical fluctuation.

Acknowledgements

We wish to thank Raul Abramo, Enzo Branchini, Xuelei Chen, Gigi Guzzo, Zhiqi Huang, Roy Maartens, Daniela Paoletti and Emiliano Sefusatti for useful discussions and suggestions. We wish to thank Olivier Doré and Roland de Putter for kindly providing the SPHEREx specifications. The support by the "ASI/INAF Agreement 2014-024-R.0 for the Planck LFI Activity of Phase E2" is acknowledged. We also acknowledge financial contribution from the agreement ASI n.I/023/12/0 "Attività relative alla fase B2/C per la missione Euclid". LM acknowledges the grants MIUR PRIN 2010-2011 "The dark Universe and the cosmic evolution

of baryons: from current surveys to Euclid" and PRIN INAF 2012 "The Universe in the box: multiscale simulations of cosmic structure". Preliminary results based on this work have been presented at the 28th Texas Symposium on Relativistic Astrophysics and at the Galileo Galilei Institute for Theoretical Physics during the workshop "Theoretical Cosmology in the Era of Large Surveys".

Note added

After this work was nearly completed, a paper forecasting Euclid-like and LSST-like capabilities [71] for models with features in the power spectrum appeared on the archive. Where a comparison is possible, our results are in qualitative agreement with those presented in [71].

References

- [1] P. A. R. Ade *et al.* [Planck Collaboration], *Astron. Astrophys.* **571** (2014) A1 [arXiv:1303.5062 [astro-ph.CO]].
- [2] R. Adam *et al.* [Planck Collaboration], arXiv:1502.01582 [astro-ph.CO].
- [3] P. A. R. Ade *et al.* [Planck Collaboration], *Astron. Astrophys.* **571** (2014) A22 [arXiv:1303.5082 [astro-ph.CO]].
- [4] P. A. R. Ade *et al.* [Planck Collaboration], arXiv:1502.02114 [astro-ph.CO].
- [5] P. A. R. Ade *et al.* [BICEP2 and Planck Collaborations], *Phys. Rev. Lett.* **114** (2015) 101301 [arXiv:1502.00612 [astro-ph.CO]].
- [6] P. A. R. Ade *et al.* [BICEP2 and Keck Array Collaborations], *Phys. Rev. Lett.* **116** (2016) 031302 [arXiv:1510.09217 [astro-ph.CO]].
- [7] C. R. Contaldi, M. Peloso, L. Kofman and A. D. Linde, *JCAP* **0307** (2003) 002 [astro-ph/0303636].
- [8] Y. S. Piao, B. Feng and X. m. Zhang, *Phys. Rev. D* **69** (2004) 103520 [hep-th/0310206].
- [9] E. Dudas, N. Kitazawa, S. P. Patil and A. Sagnotti, *JCAP* **1205** (2012) 012 [arXiv:1202.6630 [hep-th]].
- [10] A. A. Starobinsky, *JETP Lett.* **55** (1992) 489 [*Pisma Zh. Eksp. Teor. Fiz.* **55** (1992) 477].
- [11] J. A. Adams, B. Cresswell and R. Easther, *Phys. Rev. D* **64** (2001) 123514 [astro-ph/0102236].
- [12] A. Achúcarro, J. O. Gong, S. Hardeman, G. A. Palma and S. P. Patil, *JCAP* **1101** (2011) 030 [arXiv:1010.3693 [hep-ph]].
- [13] N. Bartolo, D. Cannone and S. Matarrese, *JCAP* **1310** (2013) 038 [arXiv:1307.3483 [astro-ph.CO]].
- [14] E. Silverstein and A. Westphal, *Phys. Rev. D* **78** (2008) 106003 [arXiv:0803.3085 [hep-th]].
- [15] X. Chen, R. Easther and E. A. Lim, *JCAP* **0804** (2008) 010 [arXiv:0801.3295 [astro-ph]].
- [16] R. Flauger, L. McAllister, E. Pajer, A. Westphal and G. Xu, *JCAP* **1006** (2010) 009 [arXiv:0907.2916 [hep-th]].
- [17] J. Chluba, J. Hamann and S. P. Patil, *Int. J. Mod. Phys. D* **24** (2015) no.10, 1530023 [arXiv:1505.01834 [astro-ph.CO]].
- [18] X. Chen, *Adv. Astron.* **2010** (2010) 638979 [arXiv:1002.1416 [astro-ph.CO]].
- [19] P. A. R. Ade *et al.* [Planck Collaboration], arXiv:1502.01592 [astro-ph.CO].

- [20] J. R. Fergusson, H. F. Gruetjen, E. P. S. Shellard and M. Liguori, Phys. Rev. D **91** (2015) no.2, 023502 [arXiv:1410.5114 [astro-ph.CO]].
- [21] P. D. Meerburg, M. Münchmeyer and B. Wandelt, Phys. Rev. D **93** (2016) no.4, 043536 [arXiv:1510.01756 [astro-ph.CO]].
- [22] M. J. Mortonson, C. Dvorkin, H. V. Peiris and W. Hu, Phys. Rev. D **79** (2009) 103519 [arXiv:0903.4920 [astro-ph.CO]].
- [23] P. A. R. Ade *et al.* [Planck Collaboration], arXiv:1502.01589 [astro-ph.CO].
- [24] N. Benitez *et al.* [J-PAS Collaboration], arXiv:1403.5237 [astro-ph.CO].
- [25] M. Levi *et al.* [DESI Collaboration], arXiv:1308.0847 [astro-ph.CO].
- [26] “DESI Technical Design Report Part I: Science, Targeting, and Survey Design,” <http://deso.lbl.gov/tdr>
- [27] R. Laureijs *et al.* [EUCLID Collaboration], arXiv:1110.3193 [astro-ph.CO].
- [28] L. Amendola *et al.* [Euclid Theory Working Group Collaboration], Living Rev. Rel. **16** (2013) 6 [arXiv:1206.1225 [astro-ph.CO]].
- [29] Bock, J., & SPHEREx Science Team 2016, American Astronomical Society Meeting Abstracts, 227, 147.01
- [30] O. Doré *et al.*, [arXiv:1412.4872 [astro-ph.CO]].
- [31] P. A. Abell *et al.* [LSST Science and LSST Project Collaborations], arXiv:0912.0201 [astro-ph.IM].
- [32] R. Maartens *et al.* [SKA Cosmology SWG Collaboration], PoS AASKA **14** (2015) 016 [arXiv:1501.04076 [astro-ph.CO]].
- [33] C. Gibelyou, D. Huterer and W. Fang, Phys. Rev. D **82** (2010) 123009 [arXiv:1007.0757 [astro-ph.CO]].
- [34] Z. Huang, L. Verde and F. Vernizzi, JCAP **1204** (2012) 005 [arXiv:1201.5955 [astro-ph.CO]].
- [35] J. Garriga and V. F. Mukhanov, Phys. Lett. B **458** (1999) 219 [hep-th/9904176].
- [36] J. O. Gong and M. Sasaki, Phys. Lett. B **747** (2015) 390 [arXiv:1502.04167 [astro-ph.CO]].
- [37] A. Y. Kamenshchik, A. Tronconi and G. Venturi, Phys. Lett. B **726** (2013) 518 [arXiv:1305.6138 [gr-qc]].
- [38] C. Dvorkin and W. Hu, Phys. Rev. D **81** (2010) 023518 [arXiv:0910.2237 [astro-ph.CO]].
- [39] V. Miranda and W. Hu, Phys. Rev. D **89** (2014) 8, 083529 [arXiv:1312.0946 [astro-ph.CO]].
- [40] R. Flauger, L. McAllister, E. Silverstein and A. Westphal, arXiv:1412.1814 [hep-th].
- [41] J. Martin and R. Brandenberger, Phys. Rev. D **68** (2003) 063513
- [42] M. J. D. Powell, “The BOBYQA algorithm for bound constrained optimization without derivatives,” DAMTP 2009/NA06 (2009)
- [43] H. V. Peiris *et al.* [WMAP Collaboration], Astrophys. J. Suppl. **148** (2003) 213 [astro-ph/0302225].
- [44] M. Tegmark, A. Taylor and A. Heavens, Astrophys. J. **480** (1997) 22 [astro-ph/9603021].
- [45] D. J. Eisenstein, W. Hu and M. Tegmark, Astrophys. J. **518** (1999) 2 [astro-ph/9807130].
- [46] L. Knox, Phys. Rev. D **52** (1995) 4307 [astro-ph/9504054].
- [47] G. Jungman, M. Kamionkowski, A. Kosowsky and D. N. Spergel, Phys. Rev. D **54** (1996) 1332 [astro-ph/9512139].
- [48] U. Seljak, Astrophys. J. **482** (1997) 6 [astro-ph/9608131].

- [49] M. Zaldarriaga and U. Seljak, Phys. Rev. D **55** (1997) 1830 [astro-ph/9609170].
- [50] M. Kamionkowski, A. Kosowsky and A. Stebbins, Phys. Rev. D **55** (1997) 7368 [astro-ph/9611125].
- [51] G. Nicholson and C. R. Contaldi, JCAP **0801** (2008) 002 [astro-ph/0701783].
- [52] A. Lewis, A. Challinor and A. Lasenby, Astrophys. J. **538** (2000) 473 [astro-ph/9911177].
- [53] C. Howlett, A. Lewis, A. Hall and A. Challinor, JCAP **1204** (2012) 027 [arXiv:1201.3654 [astro-ph.CO]].
- [54] S. W. Henderson *et al.*, arXiv:1510.02809 [astro-ph.IM].
- [55] T. Essinger-Hileman *et al.*, Proc. SPIE Int. Soc. Opt. Eng. **9153** (2014) 91531I [arXiv:1408.4788 [astro-ph.IM]].
- [56] S. Aiola *et al.* [LSPE Collaboration], Instrumentation 2012 Conference - Ground-based and Airborne Instrumentation for Astronomy IV, Amsterdam 1-6 July 2012, paper #8446-277 [arXiv:1208.0281 [astro-ph.IM]].
- [57] N. Kaiser, Mon. Not. Roy. Astron. Soc. **227** (1987) 1.
- [58] M. White, Y. S. Song and W. J. Percival, Mon. Not. Roy. Astron. Soc. **397** (2008) 1348 [arXiv:0810.1518 [astro-ph]].
- [59] C. Alcock and B. Paczynski, Nature **281** (1979) 358.
- [60] M. Tegmark, Phys. Rev. Lett. **79** (1997) 3806 [astro-ph/9706198].
- [61] H. A. Feldman, N. Kaiser and J. A. Peacock, Astrophys. J. **426** (1994) 23 [astro-ph/9304022].
- [62] L. R. Abramo, Mon. Not. Roy. Astron. Soc. **420** (2012) 3 [arXiv:1108.5449 [astro-ph.CO]].
- [63] R. Takahashi, M. Sato, T. Nishimichi, A. Taruya and M. Oguri, Astrophys. J. **761** (2012) 152 [arXiv:1208.2701 [astro-ph.CO]].
- [64] D. Alonso and P. G. Ferreira, Phys. Rev. D **92** (2015) no.6, 063525 [arXiv:1507.03550 [astro-ph.CO]].
- [65] L. Pozzetti *et al.*, Astron. Astrophys. **590** (2016) A3 [arXiv:1603.01453 [astro-ph.GA]].
- [66] T. Basse, J. Hamann, S. Hannestad and Y. Y. Y. Wong, JCAP **1506** (2015) no.06, 042 [arXiv:1409.3469 [astro-ph.CO]].
- [67] N. Aghanim *et al.* [Planck Collaboration], [arXiv:1507.02704 [astro-ph.CO]].
- [68] F. R. Bouchet *et al.* [CORe Collaboration], arXiv:1102.2181 [astro-ph.CO].
- [69] A. Kogut *et al.*, JCAP **1107** (2011) 025 [arXiv:1105.2044 [astro-ph.CO]].
- [70] T. Matsumura *et al.*, J. Low. Temp. Phys. **176** (2014) 733 [arXiv:1311.2847 [astro-ph.IM]].
- [71] X. Chen, C. Dvorkin, Z. Huang, M. H. Namjoo and L. Verde, arXiv:1605.09365 [astro-ph.CO].